JOURNAL OF SPACECRAFT AND ROCKETS
Vol. 42, No. 5, September–October 2005

Direct Simulation Monte Carlo Investigation of Hyperthermal Oxygen Beam Exposures

J. A. Cline*
Spectral Sciences, Inc., Burlington, Massachusetts 01803
T. K. Minton†
Montana State University, Bozeman, Montana 59717
and
M. Braunstein‡
Spectral Sciences, Inc., Burlington, Massachusetts 01803

Pulsed sources of hyperthermal O-atoms are now being extensively used to simulate low-Earth-orbit (LEO) surface exposure environments. The peak flux of these sources is many orders of magnitude larger than the corresponding LEO flux. Although it is desirable to accelerate the test by using higher fluxes than found in LEO, even commonly used fluxes are large enough to produce multicollision effects by causing a buildup of gas at the sample surface. We characterize the physical consequences to the experiment using the direct simulation Monte Carlo (DSMC) method. DSMC allows us to extract the distributions of energy and impact angle for the O-atoms that reach the surface and to record how strongly the gas buildup at the target assembly deflects flux from downstream instrumentation. By considering a range of source fluxes, we determine the onset conditions and severity of these multicollision effects. We find that, depending on the target properties, even at common experimental fluxes with a normally incident beam striking a flat surface sample, the energy distribution of incident O-atoms can broaden and develop a significant low-energy tail. The distribution of the angle of impact can also broaden significantly, and the number of O-atoms that reach downstream instrumentation can be attenuated by as much as ∼50%. These simulations will aid in the calibration of ground-based O-atom measurements and provide a model for the energy and angular distributions of O-atoms that actually impinge on surface samples.

Nomenclature

A	=	surface area
d	=	molecular collision diameter
k	=	material thermal conductivity
k_B	=	Boltzmann constant
m	=	molecular mass
n	=	number density
q	=	heat flux
T	=	temperature
v	=	velocity, or relative velocity of collision pair ij when subscripted
v'_d	=	final diffusely reflected velocity
z	=	collision frequency
λ	=	mean free path
σ	=	variable-hard-sphere collision cross section
ω	=	variable-hard-sphere collisional exponent

Introduction

In low Earth orbit, spacecraft encounter an atmosphere that, although dilute, is traversed at such high speeds that over time significant external damage is realized. The energetic impingement of atomic oxygen (AO) on external spacecraft materials causes erosion and degradation in some cases and contamination of neighboring surfaces in others.[1–3] To minimize these effects, candidate materials for space platforms are selected based on their performance in ground-based exposure experiments.

Significant attention has been devoted to accurately simulating low-Earth-orbit (LEO) exposures. The MSIS86 atmospheric model[4] describes the LEO environment at 300-km altitude as principally (79%) neutral AO with some (17%) molecular nitrogen, with a total atmospheric density of 1.14×10^{15} m^{-3} and a neutral temperature of 1124 K. The relative velocity of the impinging gas centers around the orbital velocity of 7800 m $\cdot$ s^{-1}, which, for AO, is a continuous 7.3×10^{18} m$^{-2} \cdot$ s^{-1} flux at about 5 eV. (Note: Model parameters used are for the 80th day of the year, 45° latitude, 0° longitude, 42,300 s UT, apparent solar time of noon, daily and three-month average F10.7 flux of 150, and a magnetic index of 8.)

On the ground, there are several well-developed methods for replicating the chemically aggressive hyperthermal AO component of the LEO environment.[5] Depending on the technique used, AO output can be pulsed or continuous, relatively pure or diluted with a carrier gas and/or O_2, and can have energies of 1−80 eV and fluxes from about 1/10 to more than 1000 times the atmospheric flux ($10^{18} - 10^{22}$ m$^{-2} \cdot$ s^{-1}). Such sources are used in vacuum chambers to generate a simulated LEO atmosphere to which surface-erosion test coupons are exposed.

Despite the high fidelity in energetics and chemical state[6] achieved so far in AO systems, these simulated environments still differ in some ways from LEO. For instance, LEO provides a steady flow of AO with a certain flux. To provide accelerated testing, one must increase this flux several orders of magnitude. Intuitively, if one were to keep increasing flux to a surface, one would expect at some point that the nature of the exposure would change. Gas–gas collisions between reflected and incoming beam species (multicollision effects) would begin to affect the number of beam species reaching the surface as well as their velocities and angles of impact.

One way to estimate the onset of multicollision effects is to compare the mean free path of gas–gas collisions near the target surface

Presented as Paper 2004-2685 at the AIAA 37th Thermophysics Conference, Portland, OR, 28 June–1 July 2004; received 15 July 2004; revision received 22 December 2004; accepted for publication 23 December 2004.

*Principal Scientist; jcline@spectral.com.
†Professor of Chemistry, Department of Chemistry and Biochemistry; tminton@montana.edu.
‡Group Leader, Computational Physics and Chemistry; matt@spectral.com.

to a characteristic length. The mean free path of species i passing through a mixture of species is

$$\lambda_i = v_i / z_i \tag{1}$$

where the collision frequency of species i is

$$z_i = \sum_j n_j \langle \sigma_{ij} v_{ij} \rangle \tag{2}$$

In the LEO environment at 300-km altitude, the mean free path of AO is about 2.4×10^3 m. Now consider a collimated beam of AO moving at 7.8×10^3 m $\cdot$ s^{-1} into a quiescent cloud of AO at 298 K. The cloud is the flux that can rebound from the surface under thermal accommodation. In such a case, the mean relative velocity between beam and thermalized AO is approximately 7.8×10^3 m $\cdot$ s^{-1}. If, for instance, the beam flux used in the experiment is 1000 times the LEO flux, then (neglecting chemistry) the density of the thermalized gas would at least be 1000 times that of LEO. This lower bound on AO density (10^{18} m^{-3}) gives an estimated mean free path of the fast AO of 0.1 m. Clearly, a thin layer of thermalized gas at the target could cause a significant number of energetic gas–gas collisions near the target. These collisions can create a significant effect by changing the local properties of the flux at the target. By using physics-based modeling, we hope to create a tool to characterize the multicollision effects, help troubleshoot or calibrate experiments, and interpret experimental results.

Advances in computer technology have recently made it possible to describe AO systems in detail by solving for the rarefied-gas flow using direct simulation Monte Carlo (DSMC). DSMC is a statistical method for solving the Boltzmann equation for gas flows.[7] It is particularly applicable to high Knudsen-number systems that cannot be treated by continuum methods, including both molecular beam experiments and Earth's atmosphere above 110 km. Using DSMC, we can track the time-dependent evolution of a beam pulse as it impacts, envelops, and rebounds from a sample. Next, we apply DSMC to AO experiments to elucidate the conditions seen by samples during exposure.

Because these calculations are relatively large, we cannot survey in this effort even a significant fraction of the different source flows technologically available today. Instead, we examine the general issue of multicollision phenomena in the application of LEO exposure experiments by limiting the parameter space explored to that which most directly affects the fluid mechanics. For our analysis, we vary the flux amplitude in continuous and pulsed source flows, while the other flow variables (composition, initial velocity distribution, pulse fluence) follow those of a known source.[8] Because the gas-surface interactions are not generally known for the wide variety of materials being tested, we conservatively assume a diffuse scattering model with full thermal accommodation. This assumption might overpredict multicollision phenomena for classes of materials that have specular interactions at these energies, but it allows us to begin to describe the influence of multicollision phenomena on the experimental measurements.

To our knowledge there have been no systematic experimental investigations of the multicollision effects described in this study. By simple mean free-path arguments, these effects should be readily observable under laboratory conditions. One of the purposes of this paper is to motivate laboratory studies to characterize these effects, such as those described in the Discussion section. To provide a foundation for this type of investigation, we use system parameters that are ideal and generalized. In future work some further specialization of the model to a particular system will be necessary for quantitative predictions, but the general trends and effects are evident in our current study.

Method

We use our SOCRATES implementation of Bird's DSMC method and its recently added molecular beam simulator capability.[7,9,10] SOCRATES uses a variable-hard-sphere (VHS) potential model[11] to compute collisional cross sections:

$$\sigma = \sigma_{\text{ref}} (v_{\text{ref}} / v)^{2\omega} \tag{3}$$

Table 1 VHS cross-section parameters, as evaluated from tabulated viscosity data[10,12]

Species	σ_{ref}, 10^{-19} m^2	v_{ref}, 10^3 m $\cdot$ s^{-1}	ω
N_2	3.54	2.13	0.25
O_2	3.17	1.98	0.25
O	1.75	2.49	0.25

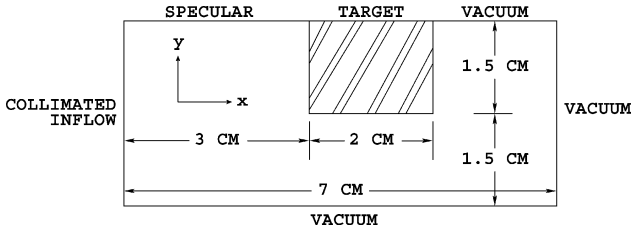

Fig. 1 Simulation domain and boundary conditions. The out-of-plane boundary conditions, not shown, are specular, to provide a quasi-two-dimensional domain.

Subscript ref denotes a reference value. Table 1 lists the VHS parameters for the species involved in these computations, which are derived from viscosity data[10,12] with the constraint that the VHS exponent ω be constant at 0.25. [Note: Our ω corresponds to the υ in Ref. 7's Eq. (2.34).]

We consider AO bombardment of a rectangular, chemically inert target that exhibits full thermal accommodation and is isothermal at 298 K. Under a simple full thermal accommodation model, all molecules that strike the surface immediately rebound from it with an average energy of $m(v'_d)^2 = 2k_B T$ in a diffusely scattered direction. As reviewed in Ref. 7 (sec. 5.8), specular isoenergetic reflections have been observed at the energies we are considering (5-eV O atoms), but full thermal accommodation is expected where adsorption can occur or at rough "engineering" surfaces. Under these constraints we expect to see the maximum influence of the target surface, so that our results represent an upper bound on the distortions caused by gas–gas multicollision phenomena.

The system is shown in Fig. 1. The flow enters from the left ($-x$) side of the domain and moves toward the right, allowing a pseudo-two-dimensional treatment. Because SOCRATES is a three-dimensional code, the bounding box is a parallelpiped and has (x,y,z) extents of (0.07,0.03,0.03) m. We consider only the end of a 0.02-m-thick target because we need high resolution to capture the flow at and around its surface. We define the origin at the target's negative edge (the lower-left corner in the figure). Because of the symmetry of the flow, specular boundary conditions are imposed at the $+y$ boundary upstream of the target surface, as well as at the z boundaries (not shown). The DSMC grid is a $36 \times 60 \times 2$ stretched-Cartesian grid of 4320 cells. The highest resolution is focused at the upstream face of the target, such that the mesh dimension there is 10^{-3} m.

The y dimension of the simulation box is large enough so that the edge effects have mostly decayed before meeting the specular symmetry boundary condition at $y = +1.5$. We determined this by enlarging the box in y until the transient high-density contour lines in front of the target met the specular boundary at 90 deg. Although the lower density contours show a longer-range edge effect, further increasing the simulation box size dramatically slows the calculation. We also neglect a subtler edge effect in which deflected flux leaving through the $-y$ boundary would normally collide with adjacent flow and reenter our domain. This domain size represents a compromise that captures the principal character of the flow without extensively enlarging the computational requirement.

The DSMC move time step used was 1.1×10^{-8} s. All simulations began with an empty box. The steady-state simulations each ran for 2300 steps before sampling started; unsteady simulations have no such run-up. Output is based on more than 5×10^5 samples in the steady-state simulations, and more than 5×10^3 samples from each of the transient calculations. Each simulation, steady and transient, used approximately 1.3×10^5 simulated molecules.

Results

From the point of view of accelerating testing, fluxes 100–1000 times those encountered in LEO are desirable for practical exposure tests. This implies average fluxes of 7.3×10^{20} to 7.3×10^{21} $m^{-2} \cdot s^{-1}$ and in pulsed systems an instantaneous flux that could be much higher depending on duty cycle, increasing the chances of gas–gas collisions upstream of and around the target. To examine this possibility, we simulate an experiment at various source fluxes to probe the onset, prominence, and impact of multicollision phenomena.

The simulations were run on Pentium-III class and higher processors under the Linux operating system, as both serial and parallel jobs (as resources were available). In aggregate, the simulation effort took tens of CPU weeks.

In the beam simulations, we use a single velocity distribution,[13] which is isosceles-triangular centered at 7.82×10^3 $m \cdot s^{-1}$ with a base width of 1.50×10^3 $m \cdot s^{-1}$. We constrain the composition of the simulated source to 2.0 O/O_2 molecule ratio. Because the beam is vacuum expanded and collimated, the constituents are assumed to be rotationally and vibrationally cold, and for all species the translational temperature in y and z is initially zero (x temperature being governed solely by the imposed triangular velocity distribution). For pulsed source simulations, the pulse is square (as it enters the simulation box) and lasts 10 μs.

When a species collides with the surface for the first time, it is tagged. We refer to the tagged molecules as "restrikes" and denote them with a superscript A in this paper. A significant restriking flux indicates that the beam molecules undergo multiple collisions at the surface.

LEO Simulation

For purposes of comparison, we first simulate the LEO environment itself. In this simulation we consider the 300-km altitude environment described earlier. We neglect minor atmospheric species and accordingly normalize the species mole fractions to 0.82 for O and 0.18 for N_2. Recall that the freestream AO flux is 7.3×10^{18} $m^{-2} \cdot s^{-1}$.

The LEO simulation results contain no surprises: the undisturbed, or freestream, fluxes and the incident (to target) fluxes match. The O flux to the target is 7.1×10^{18} $m^{-2} \cdot s^{-1}$. The restriking flux is on the order of 10^{14} $m^{-2} \cdot s^{-1}$. (Because there were so few restriking molecules in the LEO simulation, we can only report an order-of-magnitude precision on their flux.) The energy distribution of the molecules impacting the surface is Maxwellian at the expected 1124 K with a mean velocity (relative to the target body) of 7.8×10^3 $m \cdot s^{-1}$. Density at the forward-facing target surface is significantly enhanced (2.2×10^{16} m^{-3}, about a factor of 20), but the overall gas–gas collision frequency little more than doubles from the undisturbed LEO collision frequency of 5×10^{14} $m^{-3}s^{-1}$.

Continuous-Source Simulations

With the LEO scenario characterized, we now proceed with the steady-state flow system. Figure 2 shows the density of the gas for two different steady-state fluxes, 5.23×10^{20} and 5.23×10^{24} $m^{-2} \cdot s^{-1}$. The gas enters the simulation with the 2.0 O/O_2 molecule ratio and the triangular velocity distribution described in the prior section. In both cases there is a buildup of gas in front of the target, but in the low-density case those molecules collide infreqently. In the high-density case, significantly more gas–gas collisions occur, and the densified region wraps around the side of the target. Figure 3 displays the distributions of gas-surface impact energies and angles (vs normal), which again correspond to 5.23×10^{20} and 5.23×10^{24} $m^{-2} \cdot s^{-1}$. The shaded contours represent the logarithm of the flux reaching the target at the given angle and energy. In the upper frame, of lower total flux, 97% of the flux is concentrated into two very sharp peaks (centered at 5 and 10 eV for O and O_2, respectively) at normal incidence (0 deg). But in the second frame, at higher flux, the picture is completely different: the peaks are absent, and the majority of the flux strikes at random incidence angle with less than 1-eV energy.

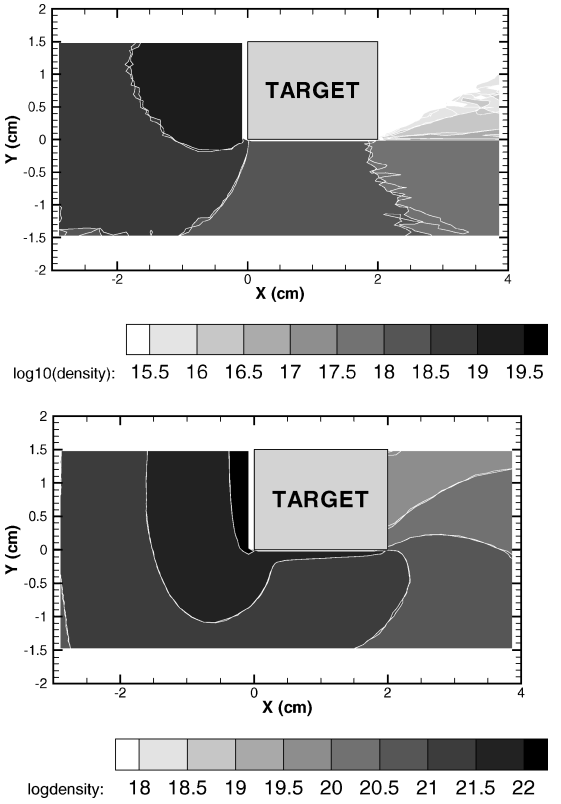

Fig. 2 Steady-state total gas density contours for nominal AO fluxes of 5.23×10^{20} (upper frame) and 5.23×10^{24} $m^{-2} \cdot s^{-1}$ (lower frame). Density units are log ($\# \cdot m^{-3}$).

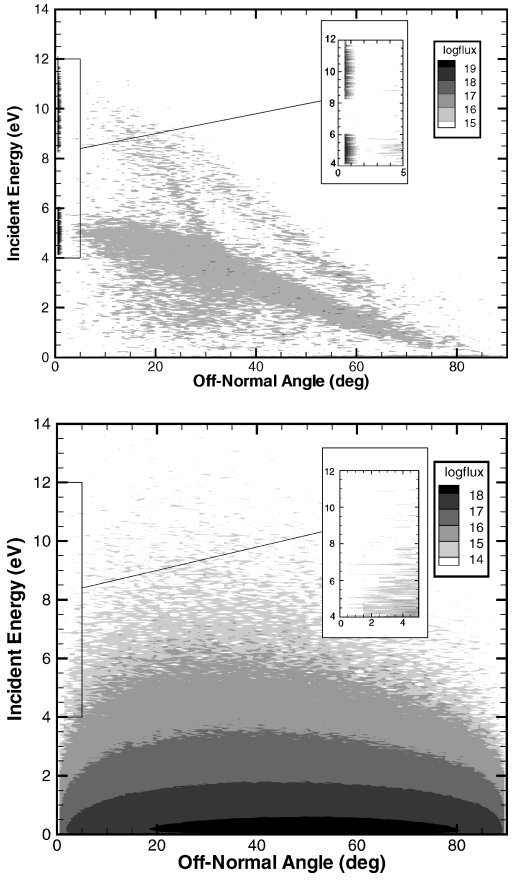

Fig. 3 Steady-state flux to the target as a function of energy and angle of incidence, same AO fluxes as in Fig. 2. The inset shows an expanded view of the 0–5-deg range within 4–12 eV. Flux units are log ($\# \cdot m^{-2} \cdot s^{-1}$).

Table 2 Number and energy flux to the target for several steady source outputs

O flux, $m^{-2} \cdot s^{-1}$			Energy flux due to AO, W/m^2		Incidence <5 deg
Nominal	Incident	Restrike	Incident	Restrike	(fraction)
5.23×10^{20}	5.05×10^{20}	5.94×10^{18}	405	2.9	0.97
5.23×10^{21}	4.83×10^{21}	5.38×10^{20}	3762	236	0.80
5.23×10^{22}	4.30×10^{22}	2.79×10^{22}	2.98×10^{4}	8182	0.37
5.23×10^{23}	3.02×10^{23}	1.03×10^{24}	1.32×10^{5}	1.60×10^{5}	0.036
5.23×10^{24}	1.17×10^{24}	1.68×10^{25}	1.66×10^{5}	1.57×10^{6}	0.0065

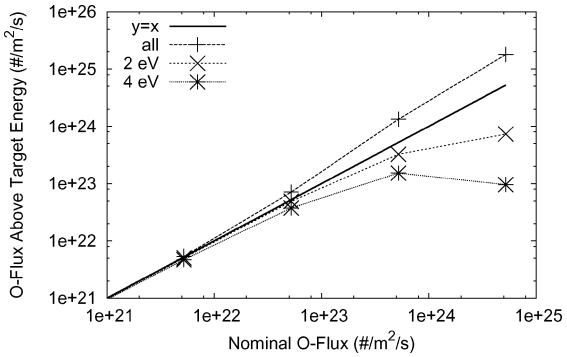

Fig. 4 Flux that impinges on the target surface above an indicated energy.

Figure 4 classifies by energy the amount of AO (both initial and restriking) that impinges upon the surface, as a function of nominal source flux. Three contours are shown: flux arriving above 4 eV, above 2 eV, and 0 eV (labeled "all"). For reference a line labeled $y = x$ illustrates where nominal flux equals flux to target. For the specific composition we use, the contour lines begin to diverge somewhere between nominal fluxes of 10^{21} and 10^{22} $m^{-2} \cdot s^{-1}$, which is between 100 and 1000 times the LEO flux, the same neighborhood that has been used for testing with continuous sources.[14–16] Table 2 summarizes our DSMC results for the flux experienced by the target as a function of nominal flux. The number flux of restriking atoms increases disproportionately as the number flux increases, while the fraction of molecules arriving at normal incidence virtually vanishes. At the higher fluxes, molecules bounce around near the target several times, so that the total flux to the surface is actually larger than the freestream flux, even as the delivered energy per molecule decreases.

The energy-dissipating behavior at higher fluxes suggests that, for exposures requiring a given energy, there is a fundamental limiting flux. For the 4-eV exposure in particular, there is a strong transition beginning between 10^{23} and 10^{24} $m^{-2} \cdot s^{-1}$ in which, despite increasing the flux by a factor of 10 or more, the $4 + eV$ flux does not correspondingly increase. The intermolecular collisions near the target surface redirect and redistribute translational energy, and for this beam composition and surface accommodation model, limit the portion of the O flux that impinges on the target at 4 eV or above to about 10^{23} $m^{-2} \cdot s^{-1}$. Such a consideration might be irrelevant to many polymers because of thermal degradation concerns (see Appendix) but is applicable when testing metals and refractory compounds.

When in the multicollision regime, the flow is changed not only at the target surface, but also downstream of it. Figure 5 shows the y profile of the flux at the downstream $(+x)$ end of the simulation box, which is 2 cm behind the target. In the figure, the statistical noise from the Monte Carlo sampling is evident and should be considered a measure of the error. As nominal flux increases, the profile changes from a step function to a continuous curve. The positive y offsets are completely hidden from the source flux by the target, but intermolecular collisions in the high-flux flows scatter significant flux behind the target.

Pulsed-Source Simulations

The pulse simulations use the same target parameters and velocity distribution as the steady simulations. Each simulation is a single

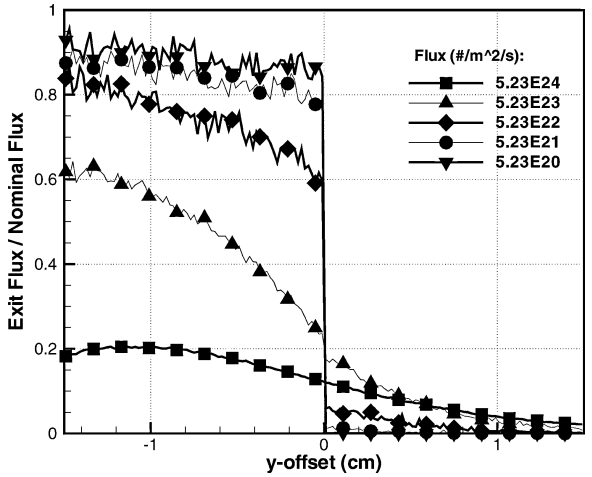

Fig. 5 Flux (relative to nominal) from a continous source that bypasses the target and exits the simulation box, as a function of its offset from the target edge ($y = 0$).

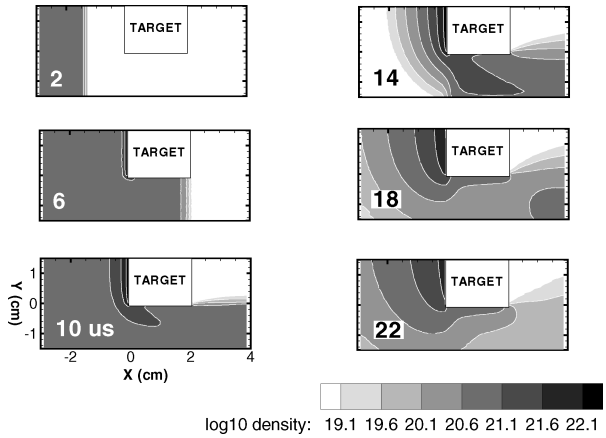

Fig. 6 Time (in μs) shapshots of the flowfield density past the target surface for a nominal O fluence per pulse of 5.22×10^{19} m^{-2}.

pulse into an evacuated chamber. We employed a square pulse shape with a constant 10-μs pulse length. The simulated time is 25 μs, with state sampling output every 1 μs. AO fluences are varied from 5.22×10^{17} to 5.22×10^{19} m^{-2} per pulse, implying O-atom pulse amplitudes from 5.22×10^{22} to 5.22×10^{24} $m^{-2} \cdot s^{-1}$, respectively.

Figure 6 shows the impact sequence (every 4 μs) for a beam with a fluence of 5.22×10^{19} m^{-2} per pulse. The shades correspond to contours of the logarithm of the total density. In addition to the development of a gas cushion upstream of the surface during the pulse, there is also a decay of slow-moving gas emanating from the surface after the pulse passes.

Figures 7–9 show the instantaneous energy fluxes caused by incident (O,O_2) and restriking (O^A, O_2^A) species. At low flux (Fig. 7), the energy is deposited evenly throughout the pulse, and almost completely by the impinging species. But in Fig. 8 there is a transition in the flow regime. At the high fluence of Fig. 9, the energy deposition rate is very nonuniform, with only the initial peak of energy delivered by incident species, and the majority is delivered through restriking collisions.

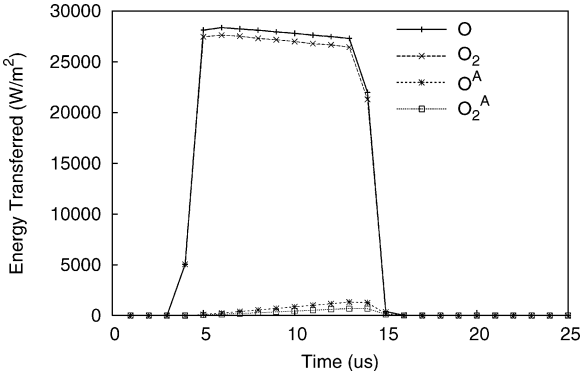

Fig. 7 Translational energy deposited into the target. Nominal O fluence per pulse: 5.22×10^{17} m^{-2}. Superscript A denotes restriking species.

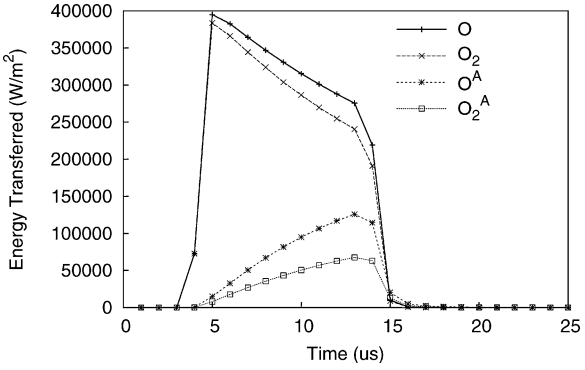

Fig. 8 Translational energy deposited into the target. Nominal O fluence per pulse: 5.22×10^{18} m^{-2}. Superscript A denotes restriking species.

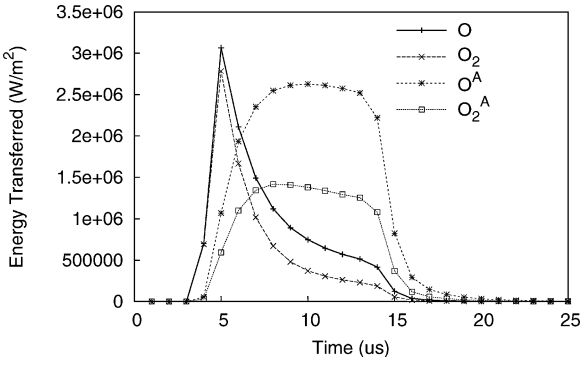

Fig. 9 Translational energy deposited into the target. Nominal O fluence per pulse: 5.22×10^{19} m^{-2}. Superscript A denotes restriking species.

In pulsed systems, there is far less gas available for buildups, so that the peak instantaneous flux can be higher than a corresponding steady-state situation without affecting impact angle or energy deposition. The low-amplitude pulse of Fig. 7 has a peak flux on the order of 10^{22}. If this were steady state, only 37% of the flux would be near normal incidence; instead, it is 90%. It requires another order of magnitude of flux before the gas accumulation interferes with incidence angle and energy. As shown in Figs. 8 and 10, the early part of the midamplitude pulse (5.22×10^{18}) arrives with nominal energy and normal incidence, then decays over time. In the large-amplitude pulse the effect is even more sudden and severe.

Last, we examine how the pulse amplitude changes how the flow scatters around and downstream of the target. Figure 11 shows the normalized pulse-integrated fluence for three pulse sizes. At 4 cm downstream from the target face (2 cm from its rear), the small-, medium-, and large-amplitude pulses develop shadows that

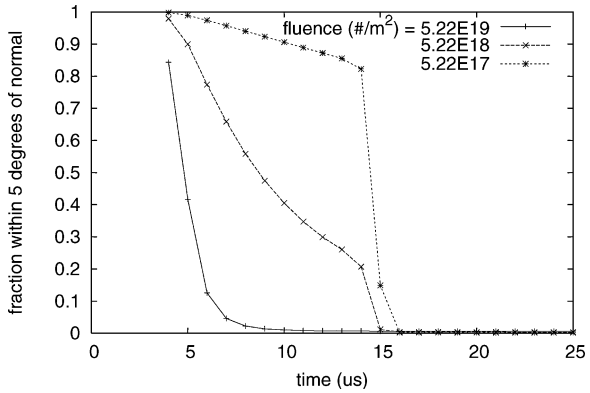

Fig. 10 Fraction of the pulsed flux striking the target within 5 deg of normal incidence, as a function of time. Integrated fractions are 0.039, 0.40, and 0.90 from highest to lowest fluence per pulse.

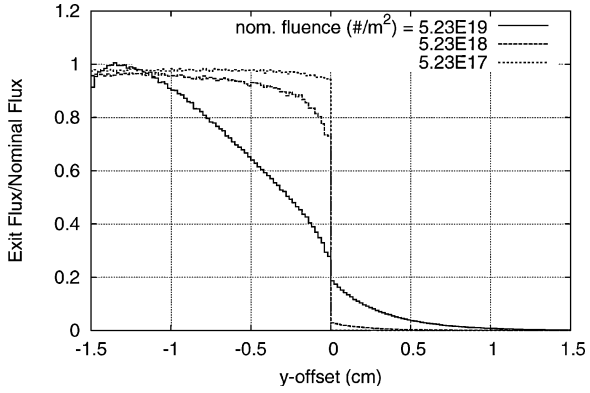

Fig. 11 Downstream flux, transient.

are, respectively, sharp, dull, and extremely diffuse. For the large-amplitude pulse, it is likely that flux measurements at a downstream detector, such as a mass spectrometer, would be quite sensitive to sample position. At the downstream end of our simulation box, changing the detector-target y offset from -5 to -2.5 mm for this case decreases the flux signal by 25%, but in this position the signal actually only represents about half of the nominal (undisturbed) amplitude.

Discussion

Fidelity to Impact Energy and Angle

Above a flux of about 10^{22} m$^{-2} \cdot$ s^{-1} (and 10^{23} for 10-μs pulsed beams), there is significant reduction in the average energy of the flux that strikes the surface. This can bring a significant fraction of the flux below the threshhold observed for certain[17] erosions, reducing the specific reactivity of the beam and making a material seem more resistant to attack. Similarly, at these conditions impact angle is also scattered over a wide range. This is not a coincidence: the more collisions a molecule sees, the more it shares its energy and randomizes its trajectory.

It has been shown that at least for polyimide the impingement angle is not relevant to the erosion chemistry.[18] But impingement angle is important to larger-scale phenomena, such as undercutting erosion,[19,20] and we might yet find systems that exhibit diffusion-limited chemistry and reactive anisotropy such that impingement angle makes a difference. But in general, beam energy is the more important parameter, and if a collimated beam hits the target with the correct energy distribution it is also likely that the impingment angle is accordingly narrowly distributed.

Downstream Flux

The flux that passes the target to downstream coincident detectors is important from the perspective of diagnostics. Foremost, it is convenient when flux can be monitored not just qualitatively but also

quantitatively as an experiment progresses, and the DSMC technique has the capability to provide such a calibration. But beyond calibration, the change in flux, in terms of amplitude as a function of nominal flux, and slope as a function of target–sensor offset, can diagnose entry into the multicollision regime.

These simulations only catalog the behavior 2 cm behind the target. In a real system with a downstream detector that might be far ($\gg$2 cm) removed from the target, there will be some broadening of the distributions reported in Figs. 5 and 11, as a result of simple propagation in noncollimated directions, and at the higher fluxes, also because of downstream intermolecular collisions. At extremely low density, the flow is collisionless, and the downstream flux profile must show a very sharp shadow. For a system that is very well characterized in terms of location of the sample, thermal accommodation coefficients, pulse lengths and shapes, velocity distribution, and other obstacles or hardware features, DSMC can quantitatively compute the variation of the flux to the detector as a function of detector position and acceptance area, and those results can be used as a calibration. But for general application, the trend elucidated by these simulations can be used to diagnose the presence of a multiple-collision regime in any system.

For instance, if source flux is known independently of the downstream detector signal (e.g., from mass flow rate and laser detonation efficiency), positioning the detector just off axis (small negative y offset) would allow detection of the multicollision regime by an inflection point in which the measured flux vs imposed deviates from linear behavior. Depending on how the background signal varies with increasing flux, positioning the detector in the positive y might also offer an option for threshold-detection of multicollision-regime entry.

Pulse Shape

In the pulse simulations there are several degrees of freedom that we did not explore, including variations in the pulse length and amplitude and variations in the velocity distribution with time or position in the pulse.

Because we introduce our beam in a constant triangular velocity distribution at the simulation boundary (3 cm from the target), the flux arrives at the target in an approximately square pulse (Fig. 12). Only about 8% of the fluence is delivered during the transients associated with starting and stopping the 10-μs pulse. The rest of the time, neglecting multicollision effects, the velocity distribution at the target is the same as the source velocity distribution.

Real systems such as the Montana State University system have an order of magnitude more distance (0.40 m) from source to target. The increased propagation time allows more velocity separation, so that the arriving pulse is broadened and rounded. In this case, virtually all of the flux is delivered in the start/stop transients. During this time, the velocity distribution to the target is changing—the earlier portion of the pulse will be made up of the faster particles and vice versa.

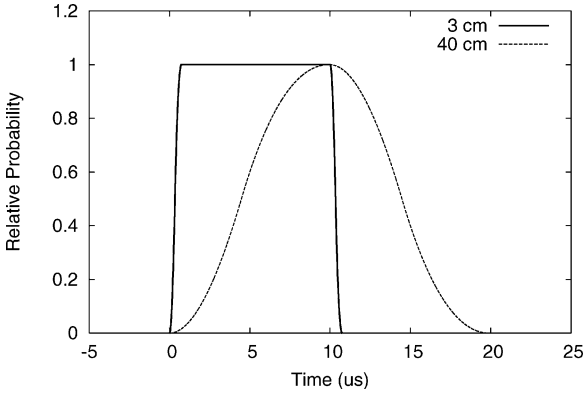

Fig. 12 Pulse shapes from an initially 10-μs square-pulsed beam after propagating 0.03 and 0.40 m (offset by 3.5 and 46.7 μs, respectively, for comparison).

This implies that the energy delivered from a more-distant pulsed molecular source might be larger than from a closer source because the higher-energy portion of the flux arrives before the density increases and the collisions dissipate energy and block flux. Also, because increased separation reduces peak instantaneous flux, systems with more-distant sources will suffer somewhat less from multicollision effects.

Pulse Amplitude/Length

Increasing pulse amplitude, as with the steady-state flux, eventually creates a multicollision environment. For the composition and 10-μs pulse length we examined, the flux can be about an order of magnitude higher in the pulsed system than in a similar steady system to achieve similar single- or multicollision behavior.

An important factor yet unexplored is the effect of pulse length. The behavior shown in Figs. 9 and 10 suggests that a much shorter pulse, for example, 1 μs, would have delivered the energy with acceptable fidelity. Conversely, if we lengthen a low-density pulse its behavior must eventually approach that of the steady-state flow system. The transition to the steady-state type of behavior might not be smooth with increasing pulse length because it involves the establishment of some structures in the flow (such as shock waves).

Application to Real Sytems

Real targets do not necessarily have a rectangular profile or even a flat surface. For example, in Fig. 13 the target, a sample holder, has bevelled edges not only at its extrema but also at each sample socket. Each sample is also retained with a durable metal screen, creating small cavities that deepen as the sample degrades under exposure.

We have only examined the external flows around the target. Presumably such features will exacerbate any multicollision phenomena already present by providing extra surfaces about which thermalized gas might linger. The extent to which this is a concern depends on many factors, including the true thermal accommodation of the surfaces and whether gaseous products are produced.

The size of the target is also a factor. Although we did not vary target size, the curvature of the density contours near the target suggests a characteristic length scale on the order of millimeters which, when approached, would reduce the gas buildup. For instance, using narrow wires or bar coupons might increase the flux at which significant multicollision phenomena begin.

A nonideality experienced in experiments is background pressure. A typical chamber pressure at the beginning of an experiment is on the order of 10^{-6} torr, which corresponds to a molecule density of about 3×10^{16} #/m^3 assuming thermal velocity (298 K). This is clearly well below the level that might cause interference. During operation, there can be excursions to 10^{-3} torr, which corresponds to a density of 3×10^{19} #/m^3, a number comparable to some of

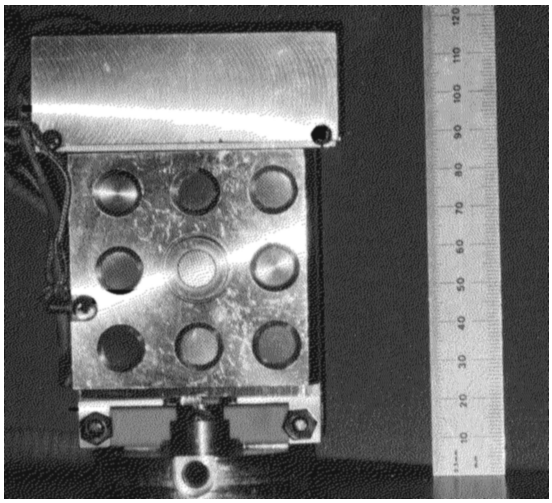

Fig. 13 Sample holder for AO exposures at Montana State University.

the beam-gas densities in this study. Unlike the beam gas at the target surface, background gas is homogeneously distributed, and its motion is not confined; its velocity is generally thermal. Given enough background gas, the collimation of the beam will be reduced.

Conclusions

By simulating in detail the interactions of steady-state and pulsed atomic-oxygen flows against a monolithic rectangular target at normal incidence, we predict the onset of multicollision phenomena at a steady-state flux above 10^{20} m$^{-2} \cdot$ s^{-1}, with severe degradation in the energy distribution fidelity above 10^{23} m$^{-2} \cdot$ s^{-1}. This onset flux will vary upwards with system-specific factors such as gas-surface interactions and true sample geometry. For pulsed systems, this behavior is similar to steady systems, but in general occurs at higher flux because gas–gas multicollision phenomena require a gas buildup that is initially absent in pulsed systems. The immediate consequences of multiple collisions in the impinging beam are dissipation of incident energy and randomization of the angle of incidence upon the target. A macroscopic consequence is that the flux to downstream detectors is deflected and spread out, most particularly at the edge of the target's flux "shadow." This behavior can in fact be used to diagnose the presence of multicollision phenomena.

Appendix: Thermal Conductivity

Depending on the sample material and how it is being cooled, a sample can pyrolize before limiting flux becomes important. Consider the one-dimensional heat-conduction equation:

$$\frac{q}{A} = k\frac{\mathrm{d}T}{\mathrm{d}x} \tag{A1}$$

The thermal conductivity of polyethylene is about 0.25 W m^{-1} K^{-1}, whereas metals are generally two to three orders of magnitude more conductive. A 1-mm-thick sample of polyethylene held at room temperature from the unexposed side will approach 300°C (and can flow or evaporate) when energy to the exposed side is about 70 kW m^{-2}, loosely corresponding to our midrange 10^{22} m$^{-2} \cdot$ s^{-1} flux. A conductive metal would need closer to 7 or 70 MW m^{-2} to achieve that temperature, and its integrity would not be threatened; this roughly corresponds to flux of 10^{25} m$^{-2} \cdot$ s^{-1}.

Acknowledgments

Work at Spectral Sciences, Inc. (SSI), was funded through a NASA Phase II Small Business Innovative Research Contract NAS8-00201 and through SSI internal research and development funds. J. A. Cline and M. Braunstein thank A. Finchum of NASA Marshall Space Flight Center for technical monitoring and guidance. Work at Montana State University was supported by the Air Force Office of Scientific Research MURI Center for Materials Chemistry in the Space Environment (AFOSR-49620-01-1-0335) and by the Department of Defense Experimental Program for the Stimulation of Competitive Research, administered by the Air Force Office of Scientific Research (AFOSR-F49620-01-1-0276).

References

[1]Arnold, G. S., "Spacecraft Contamination Model Development," *Optical Systems Contamination and Degradation*, edited by P. T. Chen, W. E. McClintock, and G. J. Rottman, *SPIE Proceedings*, Vol. 3427, 1998, pp. 272–289.

[2]Dooling, D., and Finckenor, M. M., "Materials Selection Guidelines to Limit Atomic Oxygen Effects on Spacecraft Surfaces," NASA Tech. Rept. TP-1999-209260, June 1999.

[3]Minton, T. K., and Garton, D. J., "Dynamics of Atomic-Oxygen-Induced Polymer Degredation in Low Earth Orbit," *Advanced Series in Physical Chemistry: Chemical Dynamics in Extreme Environments*, edited by R. A. Dressler, World Scientific, Singapore, 2003, pp. 420–489.

[4]Hedin, A. E., "MSIS-86 Thermospheric Model," *Journal of Geophysical Research–Space Physics*, Vol. 92, No. A5, 1987, pp. 4649–4662.

[5]Kleiman, J., Iskanderova, Z., Gudimenko, Y., and Horodetsky, S., "Atomic Oxygen Beam Sources: A Critical Overview," *Proceedings of the 9th International Symposium on Materials in a Space Environment*, ESA SP-540, Noordwijk, The Netherlands, 2003, pp. 313–324.

[6]Braunstein, M., Brunsvold, A. L., Garton, D. J., and Minton, T. K., "Measurements and Simulations of High Energy O(^3P) + Ar(^1S) Angular Scattering: Single and Multi-Collision Regimes," *Journal of Chemical Physics*, Vol. 120, No. 5, 2004, pp. 2238–2246.

[7]Bird, G. A., *Molecular Gas Dynamics and the Direct Simulation of Gas Flows*, Oxford Univ. Press, New York, 1994.

[8]Zhang, J., Garton, D. J., and Minton, T. K., "Reactive and Inelastic Scattering Dynamics of Hyperthermal Oxygen Atoms on a Saturated Hydrocarbon Surface," *Journal of Chemical Physics*, Vol. 117, No. 13, 2002, pp. 6239–6251.

[9]Braunstein, M., and Wysong, I. J., "Direct Simulation Monte Carlo Modeling of High Energy Chemistry in Molecular Beams: Chemistry Models and Flowfield Effects," *22nd International Rare Gas Dynamics Conference*, AIP Conf. Proceedings, Vol. 585, No. 1, Paper 658, American Inst. of Physics, College Park, MD, 2001.

[10]Elgin, J. B., and Bernstein, L. S., "The Theory Behind the SOCRATES Code," Geophysics Directorate, Phillips Lab., Tech. Rept. PL-TR-92-2207, Hanscom AFB, MA, Aug. 1992.

[11]Bird, G. A., *Monte Carlo Simulation in an Engineering Context*, Vol. 74, Progress in Astronautics and Aeronautics, AIAA, New York, 1981, pp. 239–255.

[12]Weast, R. C. (ed.), *CRC Handbook of Chemistry and Physics*, CRC Press, Boca Raton, FL, 1981.

[13]Cline, J. A., Buczala, D., Minton, T. K., and Braunstein, M., "Simulations of Ground and Space-Based Oxygen Atom Experiments," *Proceedings of the 9th International Symposium on Materials in a Space Environment*, ESA SP-540, Noordwijk, The Netherlands, 2003, pp. 481–485.

[14]Tennyson, R. C., "Atomic Oxygen Effects on Polymer-Based Materials," *Canadian Journal of Physics*, Vol. 69, No. 8–9, 1991, pp. 1190–1208.

[15]Cross, J. B., Koontz, S. L., and Hunton, D. E., "Flight Mass-Spectrometer Calibration in a High-Velocity Atomic-Oxygen Beam," *Journal of Spacecraft and Rockets*, Vol. 32, No. 3, 1995, pp. 496–501.

[16]Cross, J. B., and Blais, N. C., *High-Energy/Intensity CW Atomic Oxygen Beam Source*, Vol. 116, Progress in Astronautics and Aeronautics, AIAA, Washington, DC, 1989, pp. 143–155.

[17]Banks, B. A., Stueber, T., and Norris, M., "Monte Carlo Computational Modeling of the Energy Dependence of Atomic Oxygen Undercutting of Protected Polymers," NASA TM 1998-207423, April 1998.

[18]Yokota, K., Tagawa, M., and Ohmae, N., "Impingement Angle Dependence of Erosion Rate of Polyimide in Atomic Oxygen Exposures," *Journal of Spacecraft and Rockets*, Vol. 39, No. 1, 2002, pp. 155, 156.

[19]Banks, B. A., Miller, S. K. R., de Groh, K. K., and Demko, R., "Scattered Atomic Oxygen Effects on Spacecraft Materials," *Proceedings of the 9th International Symposium on Materials in a Space Environment*, ESA SP-540, Noordwijk, The Netherlands, 2003, pp. 145–152.

[20]Degroh, K. K., and Banks, B. A., "Atomic-Oxygen Undercutting of Long-Duration Exposure Facility Aluminized-Kapton Multilayer Insulation," *Journal of Spacecraft and Rockets*, Vol. 31, No. 4, 1994, pp. 656–664.

I. Boyd
Associate Editor